Identification of Active Sites of Pure and Nitrogen-Doped Carbon Materials for Oxygen Reduction Reaction Using Constant-Potential Calculations

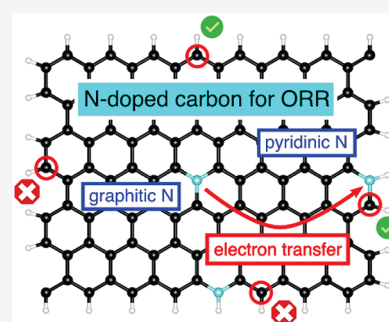Zhiyao Duan and Graeme Henkelman*

ACCESS | Metrics & More | Article Recommendations | Supporting Information

ABSTRACT: Nitrogen-doped carbon materials are promising metal-free catalysts for the electrochemical oxygen reduction reaction (ORR). A better theoretical understanding on the nature of the active site(s) would help further optimization of their ORR activity. Although quantum mechanical calculations have been widely employed to elucidate the active sites over various catalysts, these calculations are typically done assuming constant-charge conditions rather than the experimentally relevant constant-potential conditions. In this study, we employ the double-reference method to simulate the energetics of the ORR over pure and N-doped carbon materials under constant-potential conditions. We demonstrate that constant-potential calculations enable more accurate theoretical predictions, comparing well with existing experiments. Our key findings are (1) the zigzag edge of pure graphite is highly active for ORR, (2) the pyridinic N-doped armchair edge is highly active for ORR in alkaline media but not in acid, and (3) graphitic N can donate electrons to pyridinic N to enhance the ORR activity. These fundamental insights provide guidelines for the design of better carbon-based ORR catalysts.

INTRODUCTION

Low-temperature fuel cells are an attractive and promising technology to power automobiles by directly extracting electrical energy from a chemical fuel. The operation of low-temperature fuel cells requires the use of catalysts to accelerate both half-cell reactions. Pt is the most efficient and durable elemental catalyst for both anodic hydrogen oxidation reaction (HOR) and cathodic oxygen reduction reaction (ORR). As a result, expensive Pt catalysts make up a large portion of the total cost of the fuel-cell system. This cost cannot be reduced by mass production as with other components because it is due to the scarcity of Pt. Considering both the cost to consumer and the supply demand relation in the precious metal market, a target of 0.0625 g/kW for platinum-group metals (PGMs) appears appropriate, which is about a quarter of their current levels.[1] Pt-alloy catalysts[2] have shown great promise in meeting requirements for further cost reduction. For example, it has been reported that Pt-alloy catalysts have been already used in the Toyota Mirai fuel-cell electric vehicles.[3]

The ultimate goal of fuel cell catalyst research is to entirely eliminate PGMs. To this end, non-precious-metal[4] and metal-free catalysts[5] for ORR are currently under intensive research. In particular, metal-free nitrogen-doped carbon materials have been demonstrated to exhibit high ORR activities primarily in alkaline media.[6−8] Recently, carbon-based metal-free ORR catalysts have been shown to exhibit high energy efficiency and operational stability even in acidic media.[9] However, efforts are still needed to increase the power density of N-doped carbon catalysts to overcome the large required thickness of the electrodes.[1] The thick electrode induces severe transport limitations and results in poor performance at high power. To introduce more active sites per unit surface area, we must understand the local structure of the active site, which is still a topic of intense debate even after many years of research.[10,11]

The controversy focuses primarily on whether graphitic N (N_g) or pyridinic N (N_p) dopants are responsible for the activity of the ORR. Yang et al. identified that N_g at the edge of N-doped graphene could act as the active site for the ORR.[12] This is also supported by density functional theory (DFT) studies by two different groups claiming that N_g at the edge facilitates O_2 adsorption and thus promotes electron transfer to O_2.[13,14] Conversely, a recent model catalyst study examined the ORR activities of N_g-dominated and N_p-dominated highly ordered pyrolytic graphite (HOPG).[15] The results indicate that the N_p-dominated HOPG has a higher activity in comparison with that of the N_g-dominated HOPG. It was clearly shown that the ORR activity increased with increasing N_p concentration. Similarly, Wang et al. determined the ORR active center by selectively grafting acetyl groups at N_p and

ortho-carbon atoms.[16] The results indicated that the acetyl group grafted at the N_p was active because O_2 could be adsorbed and favorably reduced at the ortho-carbon atom of the pyridinic ring. The assignment of the carbon atom neighboring N_p as the active site was also supported by the detection of carbanion intermediates on N-doped carbon after ORR catalysis.[17] DFT calculations illustrate that the N_p at the edge of the carbon nanoribbons could also be the active sites for ORR.[18,19]

In this study, we present DFT calculations to elucidate the active site of ORR on pure and N-doped carbon materials. Different from previous DFT studies on the same topic, we varied the number of electrons in the system and simulated the electrochemical double layer as a function of potential in implicit solvent. In this way, we calculate the binding energies of ORR intermediates and hence ORR activities under experimentally related constant-potential conditions. Previous studies have demonstrated that constant-potential simulations can lead to dramatically different predictions as compared to typical constant-charge calculations.[20,21] Here, we use the constant-potential method to identify the active sites of ORR over pure and N-doped carbon materials. The zigzag edge is found to have high ORR active in pure carbon materials. The N_p-doped armchair edge is responsible for the high ORR activity in alkaline solution for N-doped carbons. We also found that synergistic effects between N_p and N_g dopants increase the ORR activity.

■ COMPUTATIONAL METHODS

DFT calculations with a plane-wave basis set were performed by using the Vienna *Ab initio* Simulation Package.[22−24] Electronic exchange and correlation were described by using the Perdew−Burke−Ernzerhof (PBE) functional.[25] Electron−ion interactions were described within the projector augmented wave framework.[26] In all calculations, the energy cutoff of the plane-wave basis set was 400 eV.

Slab models were employed to simulate clean and adsorbate-covered nitrogen-doped graphite surfaces. The slab models consist of five graphene layers. The middle layer was fixed during structural relaxation. The graphite basal plane was exposed on the surface. A $p(4 \times 4)$ and $2\sqrt{3} \times 4$ geometry was employed to model the supercells in the *xy*-plane. Symmetric slabs with adsorbates on both surfaces of the slab models were used to eliminate the electric dipole between the periodic surface layers. A 20 Å vacuum layer was used to eliminate interactions between periodic images in the *z*-direction. A typical slab model used in the study is shown in Figure S1. The Brillouin zone was sampled by using the Monkhorst−Pack scheme[27] with a $10 \times 10 \times 1$ *k*-point mesh. Optimized structures were obtained by minimizing the forces on each ion until they fell below 0.05 eV/Å. All calculations were non-spin-polarized because all reaction intermediates are assumed to be closed shell. Bader charge calculations were performed by using software developed by the Henkelman group.[28,29]

We employ the double-reference method to model the electrochemical metal/solution interface and to evaluate the influence of solvation and the applied potential on the reaction energetics.[30,31] The aqueous environment in this study is treated with a continuum dielectric model as implemented by the Hennig group in the VASPsol code.[32,33] A relative permittivity of 80 was set to model the aqueous electrolyte.

A value of TAU = 0 is specified to turn off the cavity setting in VASPsol. Details of the double-reference method can be found in refs 30 and 31. To model the charged interfaces at different applied potentials, for each structure, calculations were performed at charges of −2.0*e* to +2.0*e* with steps of +0.5*e*. The charged slab together with the compensating background charge polarize the electrolyte near the metal/solution interface, creating an electrostatic potential profile that simulates the EDL. The electric potential of the slab referenced to the SHE is calculated as

$$U_q \ (\text{V/SHE}) = -4.6 - \phi_q(f)/\text{eV} \tag{1}$$

where $-\phi_q(f)$ is the work function of the charged slab in aqueous media and 4.6 V is the work function of the H_2/H^+ couple at standard conditions. The total energy of the charged system is then corrected for the interaction with the background charge as well as for the difference in the number of electrons in the system by

$$E_{\text{correction}} = \int_0^q \langle \overline{V_{\text{tot}}} \rangle \, dQ + q\phi_q \tag{2}$$

The total free energy at the 11 charge values were then fit to a quadratic function to provide the free energy as a continuous function of potential. The quadratic form is consistent with a capacitor created by the charged-slab/background-charge system, which takes the form

$$E(U) = -\frac{1}{2}C(U - U_0)^2 + E_0 \tag{3}$$

where U_0 refers to the potential of zero charge (PZC), E_0 is the energy at the PZC, and C is the capacitance of the surface. From the fitted quadratic functions for the bare slab and slabs with adsorbates, the binding energies and reaction energetics as a function of electric potential were calculated.

The free energy diagram of the electrochemical ORR is constructed with the computational hydrogen electrode method.[34,35] In this method, the binding energies of three ORR intermediates (*O_2H, *O, and *OH, assuming the associative mechanism[34]) as a function of applied potential are calculated by using the potential-dependent total energies of the clean and adsorbed models. Specifically, the binding energies (ΔEs) are calculated as

$$\Delta E_{*O_2H}(U) = \frac{1}{2}(E_{*O_2H}(U) - E_*(U) - 4E_{H_2O} + 3E_{H_2}) \tag{4}$$

$$\Delta E_{*O}(U) = \frac{1}{2}(E_{*O}(U) - E_*(U) - 2E_{H_2O} + 2E_{H_2}) \tag{5}$$

$$\Delta E_{*OH}(U) = \frac{1}{2}(E_{*OH}(U) - E_*(U) - 2E_{H_2O} + E_{H_2}) \tag{6}$$

The binding energies are halved because of the symmetric slab model employed. The free energy change of each elementary step is calculated as $\Delta G = \Delta E - T\Delta S + \Delta ZPE$, where ΔZPE is the change in zero-point energy. The energies of these elementary steps (ΔE) are the energy differences between the DFT-calculated energies of the product and reactant states. The chemical potential of the solvated proton and electron pair ($H^+ + e^-$) at standard conditions (pH = 0, T = 298.15 K) is calculated as $^1/_2 G_{H_2} + eU_{\text{SHE}}$ assuming equilibrium at the

standard hydrogen electrode. The changes in ΔZPE and $T\Delta S$ are calculated by using previously determined values.[34] The sensitivity of the implicit solvation model on the binding energies of the ORR intermediates was tested on the Pt(111) surface. The solvation energies for *OH and *O$_2$H adsorbed on Pt(111) are calculated to be −0.34 and −0.47 eV. In comparison, the solvation energy of *OH calculated by using a water bilayer model has been determined to be in the range of −0.33 eV[34,35] and −0.57 eV.[36] For *O$_2$H, the water bilayer model predicts a solvation energy of −0.49 eV, which is close to our implicit solvent value. Thus, the implicit solvation model appears to provide a reasonable estimation of the solvation energy for ORR intermediates

The pH can also affect the adsorption energies of reaction intermediates by effectively changing the electric potential. Indeed, by changing the pH value, the electric potential on the standard hydrogen electrode (SHE) scale also changes at fixed potential on the reversible hydrogen electrode (RHE) scale according to the relation

$$U_{RHE} = U_{SHE} + k_B T \ln(10) \text{pH}/e \qquad (7)$$

In this study, we evaluate pH-dependent ORR activities on the RHE scale by calculating binding energies at the corresponding SHE potentials.

■ RESULTS AND DISCUSSION

ORR Activities of Graphite and N-Doped Graphite. We have systematically examined the ORR activities at different active sites on graphite and N-doped graphite. The local atomic structures of the examined active sites are shown in Figure 1. The active sites considered include zigzag edge of
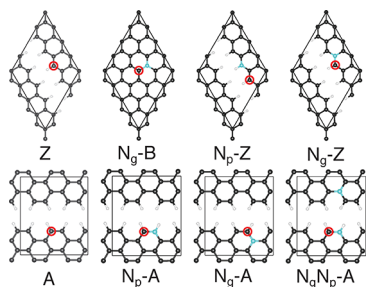

Figure 1. Atomic structures of different active sites. The color code is black for C, cyan for N, and white for H. The sites where ORR intermediates bind are marked with red circles.

graphite (Z), armchair edge of graphite (A), N$_g$-doped basal plane (N$_g$-B), N$_p$-doped zigzag edge (N$_p$-Z), N$_g$-doped zigzag edge (N$_g$-Z), N$_p$-doped armchair edge (N$_p$-A), and N$_g$-doped armchair edge (N$_g$-A). Finally, we use an N$_g$ and N$_p$ codoped armchair edge (N$_g$N$_p$-A) model to study the interaction between N$_g$ and N$_p$. We also examined the carbon site at the nondoped basal plane of graphite. However, we found that *O$_2$H cannot stably bind on this site, so it is not further discussed. Similarly, the C atoms close to the edges with 3C and 2C1N coordination were all found to have very weak adsorption energies, so they are also not discussed further. Pyrrolic N (N bonded to two C and one H in a five-membered ring) also exists in N-doped C catalysts. The concentration of pyrrolic N is usually very low due to its highly strained carbon environment in carbon materials dominated by six-membered C rings. Hence, we exclude pyrrolic N in our study. There is

also an interest in elucidating whether N$_p$ or N$_g$ is the active site.[15] Another possible concern regarding our atomic models is that the two edges in our models are too close due to the limited size of the supercell. We did, however, observe that the surface carbon ribbons tilted after relaxation, and so the distance between the two edges is increased in the z-direction. Additionally, the ORR activities are determined by the adsorption energies of ORR intermediates, which are in turn determined by the relative energies between the adsorbed model and bare model. Hence, we expect the interaction between the two edges to largely cancel.

An uncertainty of the atomic structures of N$_p$-doped zigzag and armchair edges is if N$_p$ is hydrogenated or not. To answer this question, we calculated the free energy of hydrogenation ($\Delta G_H = E_{N_p-H} - E_{N_p} - {}^1\!/_2\mu_{H_2} + eU$) at the zigzag and armchair edges. The results are shown in Figure S2 of the Supporting Information. Because the ΔG_H's are negative over the ORR-related potential range, we employed hydrogenated models to study their ORR activity.

The ORR activities of various active sites were characterized by using the above-presented method. Here, we show the details of the calculations using the N$_g$-B site. Figure 2 shows the atomic structure of N$_g$-B, the total energies as a function of potential, the binding energies as a function of potential, and the free energy profile of ORR at pH = 1 and pH = 13. It can be seen in Figure 2b that the potential-dependent total energies are well-represented by the parallel capacitor model. After the adsorption of oxygenated species, the PZCs of adsorbed interfaces move up due to the electron transfer from electrode to the adsorbates, which increases the work function of the electrode. Consequently, the binding energies of the oxygenated species strongly depend on the applied potential. Specifically, the binding energies become stronger when the applied electrode potential is lowered, as shown in Figure 2c. This indicates that the binding energies get stronger at higher pH according to eq 7. The free energy diagrams of ORR at pH = 1 and pH = 13 are evaluated based on the potential-dependent binding energies as shown in Figures 2d and 2e, respectively. The theoretical onset potential at pH = 1 is as low as 0.08 V/RHE due to weak adsorption of *O$_2$H. At pH = 13, the onset potential of 0.39 V/RHE becomes only somewhat higher as a result of stronger adsorption.

The ORR activities of other active sites at pH = 1 and pH = 13 are summarized in Figure 3. The computational details are shown in Figures S3−S9.

The zigzag edge of nondoped graphite exhibits high ORR activities in both acid and base. The theoretical onset potentials at pH = 1 and pH = 13 are calculated to be 0.6 and 0.7 V/RHE, respectively. In acidic media, the reduction of *OH to water is the potential-limiting step. In base, the *O$_2$H formation step determines the onset potential. Comparatively, at the armchair edge of graphite, the *O$_2$H adsorption is too weak under the operating potentials of the ORR, leading to poor ORR activities in both acidic and alkaline solutions. The weak adsorption at the armchair edge is caused by the strong C−C bonding between the two undercoordinated C atoms at the edge. The bond length is 1.37 Å, which is shorter than 1.41 Å of the C−C bond at the zigzag edge (see Figures S3 and S4). Consequently, the C atom at the zigzag edge is more active than that at the armchair edge.

The N doping at the zigzag edge is found to have negative effects on the ORR activity. First, the N$_p$ dopants directly
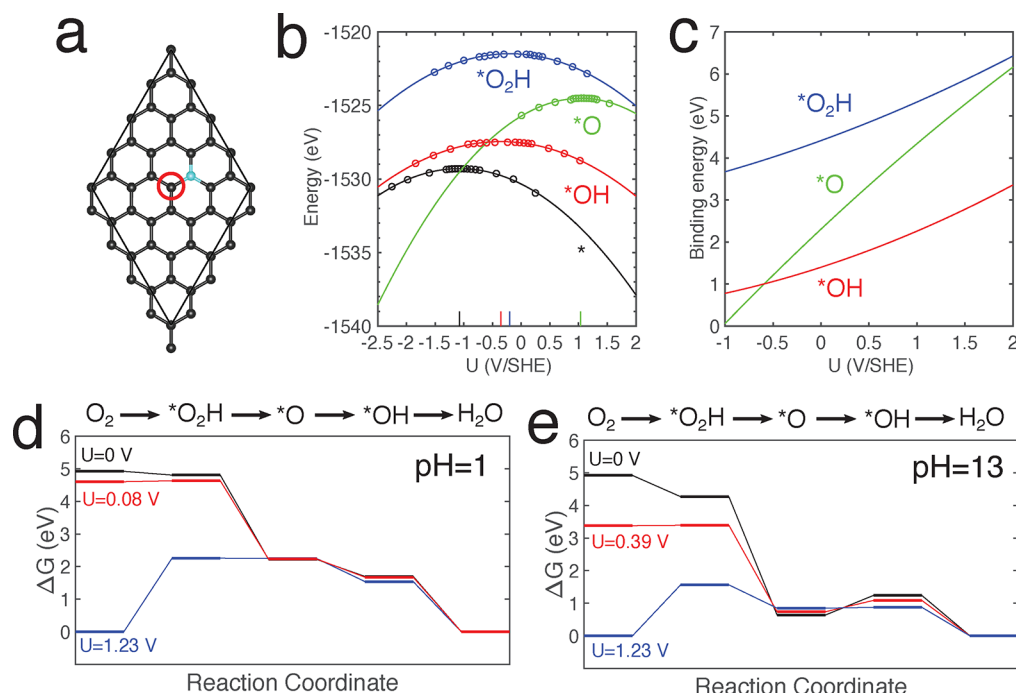
Figure 2. (a) Atomic structure of N_g-B. The active site is marked by the red circle. (b) Total energies of bare (black), $*O_2H$ (blue), $*O$ (green), and $*OH$ (red) as a function of applied potential U. Calculated total energies (circles) and polynomial fits (solid lines) are shown. (c) Binding energies of $*O_2H$ (blue), $*O$ (green), and $*OH$ (red) as a function of U. (d) Free energy diagrams of the ORR at pH = 1. (e) Free energy diagrams of the ORR at pH = 13.
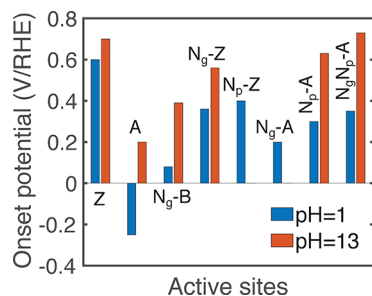

Figure 3. Predicted onset potentials for various active sites at pH = 1 and pH = 13.

occupy the most active sites at the nondoped zigzag edge. The N_p dopants also deactivate the neighboring C sites at the zigzag edge (N_p-Z). The onset potential of ORR for the N_p-Z site is predicted to be 0.4 and 0 V/RHE at pH = 1 and = 13, respectively, which are significantly lower than those without the neighboring N_p. Structurally, N_p enhances the C–C bonding of the neighboring C atoms, which is evidenced by the shorter C–C bond length of 1.39 Å as compared to 1.41 Å without N_p (see Figure S6).

The ORR activity of N_g-Z is higher than that of N_p-Z but still lower than the nondoped carbon. The ORR onset potentials of the N_g-Z at pH = 1 and pH = 13 are predicted to be 0.36 and 0.56 V/RHE, respectively. The reduced activity of N_g-Z is due to the overstabilization of $*O$ and $*OH$, leading to difficulties in the reduction of $*OH$. We also computationally characterize the ORR activity of a next nearest-neighboring C site at the zigzag edge from the N_g. The results are presented in Figure S10. The activity of this site gets closer to the nondoped zigzag edge but is still lower. Hence, the negative influence of N_g can at least reach the next nearest-neighbor C site at the zigzag edge.

With regard to the N-doped armchair edge, the N_g dopant cannot activate the neighboring C site for ORR. The site still suffers from insufficient binding strengths of the oxygenated species. The result can be understood by the even shorter C–C bond length at the armchair edge after N_g dopant. Specifically, the bond length varies from 1.37 to 1.36 Å after N_g doping (see Figure S7).

On the other hand, the N_p dopant can effectively activate the C site at the armchair edge. At pH = 13, the onset potential of ORR is 0.63 V/RHE, which is a substantial enhancement (a 400 mV shift) over the nondoped material. In acidic media, the onset potential is only 0.3 V/RHE. The strong pH-dependent activity is attributed to the potential-dependent binding energies of oxygenated species, which quickly increase with increasing electrode potential as shown in Figure S8. The high activity of N_p-A can be understood by the change of C=C at the armchair edge to the much weaker C–N bond. Indeed, the bond dissociation energy of CH_3–NH_2 is 79 kcal/mol, which is less than half of that of the H_2C=CH_2 bond (167 kcal/mol).[37]

Synergy between Graphitic and Pyridinic N Dopants. Although we have demonstrated that the N_p dopant can activate the armchair edge and results in good ORR activity in alkaline media, the predicted onset potential of 0.63 V/RHE is still significantly lower than the experimental value of about 0.8 V/RHE.[6] Considering the N-doped carbon materials normally consist of both N_g and N_p dopants at the same time, we set out to examine the electronic interaction between them, which could lead to further enhancement of the ORR activity of N_p-A. This hypothesis is backed by previous studies concluding that n-type doping was found for N_g and p-type doping for N_p.[38] Hence, we expect electron transfer from N_g to N_p when they coexist in the N-doped carbon materials. The hypothesis is examined by using the N_g and N_p codoped model as

presented in Figure 1 (N_gN_p-A), in which the N_g is placed far from the N_p, so they do not have direct interactions but only electronic ones.

Interestingly, our calculation does show that the onset potential of ORR for N_gN_p-A at pH = 13 is further increased by 100 mV as compared to the N_p-A. The enhancement can be attributed to the stronger binding of *O_2H as shown in Figure 4. The Bader charge analysis in Figure 5 shows that there is
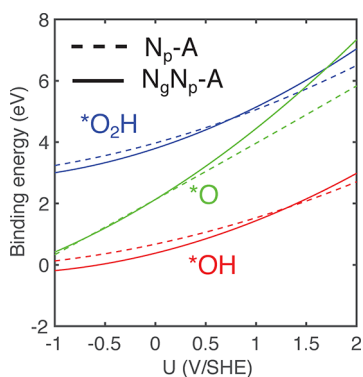

Figure 4. Comparison between binding energies of ORR intermediates on N_p-A and N_gN_p-A.

electron transfer from the N_g to the N_p when they are codoped. Specifically, it can be seen that the Bader charge of N_p increases from $-2.87e$ to $-2.92e$ before and after N_g codoping. Correspondingly, the Bader charge of the N_g decreases from $-2.75e$ to $-2.66e$. The projected density of states (pDOS) also show that N_g-doped graphite has a higher Fermi energy as compared to that of the N_p-doped graphite, which supports the direction of electron transfer from N_g to N_p. Bader charges of all atoms on the surfaces are shown in Figure S11.

The electron transfer obviously disturbs the C$-N_p$ bonding at the armchair edge. This is manifested by the bond length changes as shown in Figure 5. The C$-$N bond length elongates from 1.345 to 1.355 Å after codoping, which indicates a weakening of the C$-$N bond. Observing the pDOS of the

codoped model, we can see that two sharp peaks appear at -9 and -3 eV in the pDOS of N_p. The pDOS of the singly doped N_p is multipeaked and more flat at the same energy range, indicating stronger C$-$N interactions. From these observations, it is proposed that the electron transfer from N_g to N_p weakens the C$-N_p$ bond because the N_p atom shares or acquires less electron density from the C atom.

Comparison with Experiment. The theoretical predictions above are compared with experiments in this section. First, we have identified that the zigzag edge of the nondoped graphite is highly ORR active. The predicted theoretical onset potential is 0.7 V/RHE at pH = 13 and 0.6 V/RHE at pH = 1. This finding seems contradictory to most experimental studies, where only the N-doped carbon materials are considered active.[6,7,15] However, in a recent study, Xue et al. partially unzipped the multiwall carbon nanotube which resulted in a well-defined zigzag edge along the obtained graphene nano-ribbons.[39] The ORR activity of the zigzag edge has been demonstrated to be high with an onset potential of 0.960 V and a half-wave potential of 0.819 V. In acidic media, the catalyst also has considerable ORR activity with an onset potential of 0.760 V and a half-wave potential of 0.633 V. These observations are qualitatively consistent with our calculations. The difference of the onset potential numbers between theory and experiment could be due to the different definitions. In theory, the onset potential is defined by the highest potential where all reaction steps are exothermic.[34] Actually, the ORR can occur above this potential as a result of thermal activation when certain elementary steps are slightly endothermic. Thus, the theoretical onset potential could be better compared to the experimental half-wave potential.

We have also identified that $N_p$$-$A is the active site for N-doped carbon materials. The important role of N_p dopants in activating carbon materials for ORR has been highlighted by various experimental studies.[15,16,40] In this study, we elaborate on these experimental findings with atomic details that only N_p at the armchair edge is responsible for the high activity of N-doped carbon. Essentially, this is because the C$=$C bond can be activated when one of the C atoms is replaced with
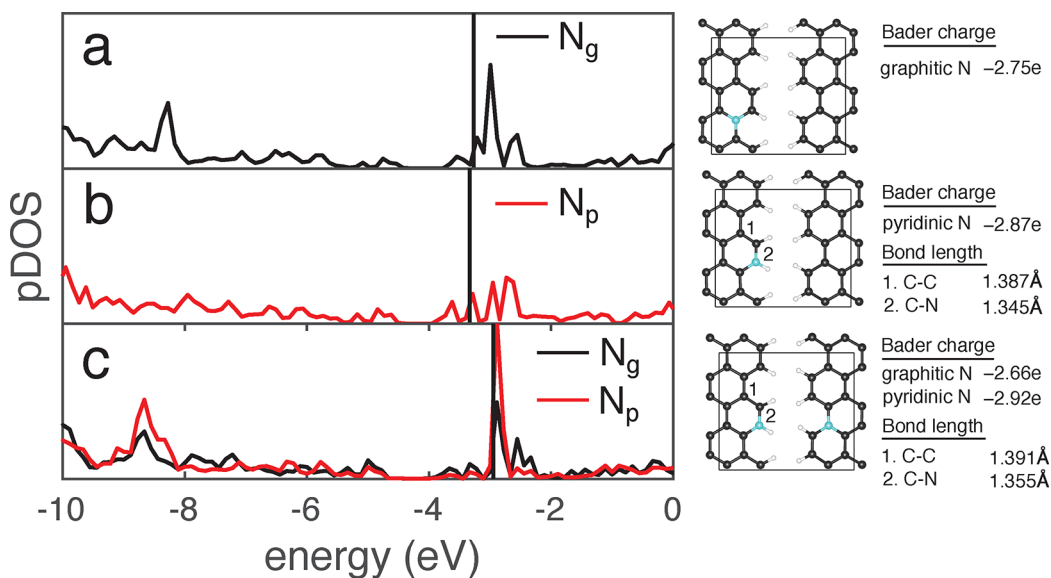

Figure 5. Projected density of states (pDOS) of N dopants and Bader charge analysis for (a) N_g-A, (b) N_p-A, and (c) N_gN_p-A. The zero energy in the pDOS plots is set to the vacuum level.
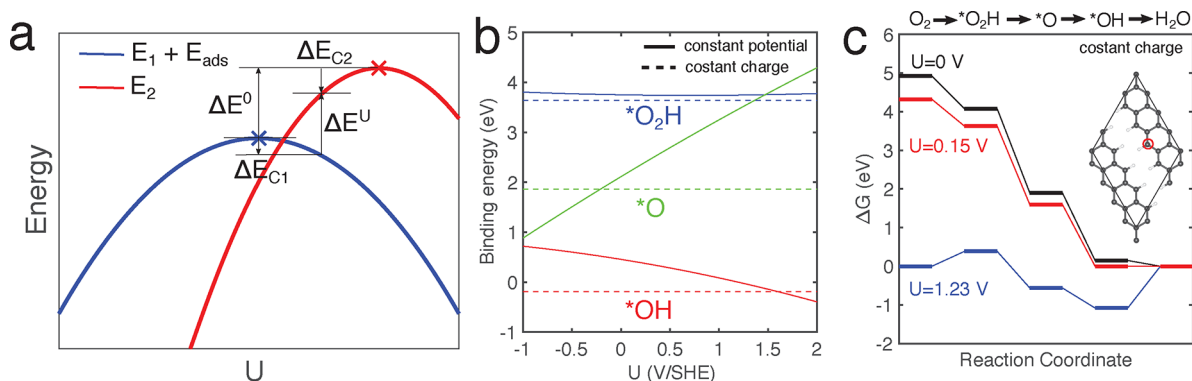
Figure 6. (a) Schematic illustration of the relation between binding energies at constant-charge and constant-potential conditions. (b) Comparison between binding energies of the ORR intermediates at the zigzag edge calculated under constant-charge and constant-potential conditions. (c) Free energy diagrams of the ORR at the zigzag edge under constant-charge conditions.

hydrogenated N, resulting in a weaker $C-N_p$ bond. Experimentally, different N_p containing molecules deposited on carbon black are used to explore the optimal N configurations for ORR activity (Figure 6 in ref). We noticed that molecules having armchair-like local structures such as phenanthroline (⬡⬡⬡) are much more active than those bearing zigzag-like structures such as phenazine (⬡⬡⬡).

Moreover, the widely observed pH-dependent ORR activities[9,39] of N-doped carbon can be explained by the potential-dependent binding energies. For the most active N_p-A and N_gN_p-A sites, the binding energies of the oxygenated species increase with increasing electrode potentials (see Figures S8 and S9). Thus, in alkaline media, the binding strengths are much stronger than those in acid electrolyte leading to more facile activation of the O−O bond, which is essential for a high onset potential and the four-electron reaction pathway. For the nondoped zigzag edge, the ORR activity only mildly depends on the pH of the electrolyte,[39] which can also be explained by the less sensitive $*O_2H$ and $*OH$ binding energies to the electrode potential, as shown in Figure S3.

Finally, we found that N_g dopants are not just spectators and that they transfer electrons to the N_p dopants at the armchair edge and further enhance the ORR activity of N_p-A. This synergistic effect between N_g and N_p has recently been observed in experiments.[41] In the study, the ratio of N_p to N_g was continuously tuned, and the corresponding ORR activities were characterized. It has been demonstrated that the ORR activity reaches the highest when $[N_p]:[N_g]$ equals 1.4.

Constant-Charge vs Constant-Potential Simulation. Because the binding energies calculated under constant-charge condition are widely used for predicting ORR activities, it is of interest to compare them with the constant-potential binding energies and elucidate the difference. To this end, we assume the total energies of the electrochemical interfaces before and after adsorption are E_1 and E_2, respectively. According to eq 3, E_1 and E_2 can be written as $-1/2 C_1 (U - U_1^0)^2 + E_1^0$ and $-1/2 C_2 (U - U_2^0)^2 + E_2^0$, respectively. We write the energy of capacitor as $\Delta E_C \equiv -1/2 C (U - U^0)^2$ for simplicity. The binding energy at a certain potential U can be calculated as

$$\Delta E^U = E_2 - E_1 - E_{ads}$$
$$= \Delta E_{C2} - \Delta E_{C1} + (E_2^0 - E_1^0 - E_{ads})$$
$$= \Delta E_{C2} - \Delta E_{C1} + \Delta E^0 \tag{8}$$

where E_{ads} is the energy of the isolated adsorbate and ΔE^0 is the binding energy at constant zero charge. Hence, $\Delta E^U - \Delta E^0 = \Delta E_{C2} - \Delta E_{C1}$ relies on the energy difference between the two capacitors before and after adsorption. The adsorbate normally changes the PZC and the capacitance of the electrochemical interface, resulting in nonzero difference between binding energies at constant-charge and constant-potential conditions. In Figure 6a, we show this difference schematically and that the difference can lead to a substantial impact on the binding energies, as shown in Figure 6b, using the adsorption of ORR intermediates at the zigzag edge of graphite as an example. Using the binding energies calculated under constant-charge conditions to build the free energy diagrams of ORR as shown in Figure 6, we predicted the zigzag edge to have very low ORR activity, which is inconsistent with experiment. Moreover, the constant-charge binding energies do not vary with applied potentials; thus, the pH-dependent activity cannot understood theoretically.

◼ CONCLUSION

In summary, we provide fundamental insights into the ORR active sites over pure carbon and N-doped carbon materials by employing DFT calculations under experiment-relevant constant-potential conditions. Our findings compare well with experiments and provide suggestions to further improve the ORR activity of N-doped carbon materials. Our work also highlights that the importance of considering constant-potential conditions in the calculations since the applied potential has a strong modulation on the binding energies of ORR intermediates, which are not captured by typical constant-charge calculations.

◼ ASSOCIATED CONTENT

ⓢ Supporting Information

The Supporting Information is available free of charge at https://pubs.acs.org/doi/10.1021/acs.jpcc.0c03951.

> Atomic models, free energy of hydrogenation reaction of pyridic N at graphite edges, potential-dependent adsorption energies, pH-dependent ORR activities at various active sites, and Bader changes (PDF)

◼ AUTHOR INFORMATION

Corresponding Author

Graeme Henkelman − *Department of Chemistry and the Oden Institute for Computational Engineering and Sciences, The*

University of Texas at Austin, Austin, Texas 78712-0165,
United States; ⊙ orcid.org/0000-0002-0336-7153;
Email: henkelman@utexas.edu

Author

    Zhiyao Duan − *Department of Chemistry and the Oden Institute
for Computational Engineering and Sciences, The University of
Texas at Austin, Austin, Texas 78712-0165, United States*

Complete contact information is available at:
https://pubs.acs.org/10.1021/acs.jpcc.0c03951

Notes

The authors declare no competing financial interest.

■ ACKNOWLEDGMENTS

■ REFERENCES

(1) Kongkanand, A.; Mathias, M. F. The Priority and Challenge of High-Power Performance of Low-Platinum Proton-Exchange Membrane Fuel Cells. *J. Phys. Chem. Lett.* **2016**, *7*, 1127−1137.

(2) Stephens, I. E. L.; Bondarenko, A. S.; Grønbjerg, U.; Rossmeisl, J.; Chorkendorff, I. Understanding the electrocatalysis of oxygen reduction on platinum and its alloys. *Energy Environ. Sci.* **2012**, *5*, 6744−6762.

(3) Konno, N.; Mizuno, S.; Nakaji, H.; Ishikawa, Y. Development of Compact and High-Performance Fuel Cell Stack. *SAE Int. J. Alt. Power.* **2015**, *4*, 123−129.

(4) Gewirth, A. A.; Varnell, J. A.; DiAscro, A. M. Nonprecious Metal Catalysts for Oxygen Reduction in Heterogeneous Aqueous Systems. *Chem. Rev.* **2018**, *118*, 2313−2339.

(5) Dai, L.; Xue, Y.; Qu, L.; Choi, H.-J.; Baek, J.-B. Metal-Free Catalysts for Oxygen Reduction Reaction. *Chem. Rev.* **2015**, *115*, 4823−4892.

(6) Gong, K.; Du, F.; Xia, Z.; Durstock, M.; Dai, L. Nitrogen-Doped Carbon Nanotube Arrays with High Electrocatalytic Activity for Oxygen Reduction. *Science* **2009**, *323*, 760−764.

(7) Qu, L.; Liu, Y.; Baek, J.-B.; Dai, L. Nitrogen-Doped Graphene as Efficient Metal-Free Electrocatalyst for Oxygen Reduction in Fuel Cells. *ACS Nano* **2010**, *4*, 1321−1326.

(8) Wang, X.; Lee, J. S.; Zhu, Q.; Liu, J.; Wang, Y.; Dai, S. Ammonia-Treated Ordered Mesoporous Carbons as Catalytic Materials for Oxygen Reduction Reaction. *Chem. Mater.* **2010**, *22*, 2178−2180.

(9) Shui, J.; Wang, M.; Du, F.; Dai, L. N-doped carbon nanomaterials are durable catalysts for oxygen reduction reaction in acidic fuel cells. *Sci. Adv.* **2015**, *1*, e1400129.

(10) Singh, S. K.; Takeyasu, K.; Nakamura, J. Active Sites and Mechanism of Oxygen Reduction Reaction Electrocatalysis on Nitrogen-Doped Carbon Materials. *Adv. Mater.* **2019**, *31*, 1804297.

(11) Shao, Y.; Jiang, Z.; Zhang, Q.; Guan, J. Progress in Nonmetal-Doped Graphene Electrocatalysts for the Oxygen Reduction Reaction. *ChemSusChem* **2019**, *12*, 2133−2146.

(12) Yang, H. B.; Miao, J.; Hung, S.-F.; Chen, J.; Tao, H. B.; Wang, X.; Zhang, L.; Chen, R.; Gao, J.; Chen, H. M.; Dai, L.; Liu, B. Identification of catalytic sites for oxygen reduction and oxygen evolution in N-doped graphene materials: Development of highly efficient metal-free bifunctional electrocatalyst. *Sci. Adv.* **2016**, *2*, e1501122.

(13) Kim, H.; Lee, K.; Woo, S. I.; Jung, Y. On the mechanism of enhanced oxygen reduction reaction in nitrogen-doped graphene nanoribbons. *Phys. Chem. Chem. Phys.* **2011**, *13*, 17505−17510.

(14) Li, M.; Zhang, L.; Xu, Q.; Niu, J.; Xia, Z. N-doped graphene as catalysts for oxygen reduction and oxygen evolution reactions: Theoretical considerations. *J. Catal.* **2014**, *314*, 66−72.

(15) Guo, D.; Shibuya, R.; Akiba, C.; Saji, S.; Kondo, T.; Nakamura, J. Active sites of nitrogen-doped carbon materials for oxygen reduction reaction clarified using model catalysts. *Science* **2016**, *351*, 361−365.

(16) Wang, T.; Chen, Z.-X.; Chen, Y.-G.; Yang, L.-J.; Yang, X.-D.; Ye, J.-Y.; Xia, H.-P.; Zhou, Z.-Y.; Sun, S.-G. Identifying the Active Site of N-Doped Graphene for Oxygen Reduction by Selective Chemical Modification. *ACS Energy Lett.* **2018**, *3*, 986−991.

(17) Xing, T.; Zheng, Y.; Li, L. H.; Cowie, B. C. C.; Gunzelmann, D.; Qiao, S. Z.; Huang, S.; Chen, Y. Observation of Active Sites for Oxygen Reduction Reaction on Nitrogen-Doped Multilayer Graphene. *ACS Nano* **2014**, *8*, 6856−6862.

(18) Zhang, L.; Xia, Z. Mechanisms of Oxygen Reduction Reaction on Nitrogen-Doped Graphene for Fuel Cells. *J. Phys. Chem. C* **2011**, *115*, 11170−11176.

(19) Ferre-Vilaplana, A.; Herrero, E. Understanding the chemisorption-based activation mechanism of the oxygen reduction reaction on nitrogen-doped graphitic materials. *Electrochim. Acta* **2016**, *204*, 245−254.

(20) Kim, D.; Shi, J.; Liu, Y. Substantial Impact of Charge on Electrochemical Reactions of Two-Dimensional Materials. *J. Am. Chem. Soc.* **2018**, *140*, 9127−9131.

(21) Duan, Z.; Henkelman, G. Theoretical Resolution of the Exceptional Oxygen Reduction Activity of Au(100) in Alkaline Media. *ACS Catal.* **2019**, *9*, 5567−5573.

(22) Kresse, G.; Hafner, J. Ab Initio Molecular Dynamics for Liquid Metals. *Phys. Rev. B: Condens. Matter Mater. Phys.* **1993**, *47*, 558.

(23) Kresse, G.; Furthmüller, J. Efficiency of Ab-Initio Total Energy Calculations for Metals and Semiconductors Using a Plane-Wave Basis Set. *Comput. Mater. Sci.* **1996**, *6*, 15−50.

(24) Kresse, G.; Furthmüller, J. Efficient Iterative Schemes for Ab Initio Total-Energy Calculations Using a Plane-Wave Basis Set. *Phys. Rev. B: Condens. Matter Mater. Phys.* **1996**, *54*, 11169.

(25) Perdew, J. P.; Burke, K.; Ernzerhof, M. Generalized Gradient Approximation Made Simple. *Phys. Rev. Lett.* **1996**, *77*, 3865−3868.

(26) Blöchl, P. E. Projector augmented-wave method. *Phys. Rev. B: Condens. Matter Mater. Phys.* **1994**, *50*, 17953−17979.

(27) Monkhorst, H. J.; Pack, J. D. Special Points for Brillouin-Zone Integrations. *Phys. Rev. B* **1976**, *13*, 5188−5192.

(28) Henkelman, G.; Arnaldsson, A.; Jónsson, H. A fast and robust algorithm for Bader decomposition of charge density. *Comput. Mater. Sci.* **2006**, *36*, 354−360.

(29) Tang, W.; Sanville, E.; Henkelman, G. A grid-based Bader analysis algorithm without lattice bias. *J. Phys.: Condens. Matter* **2009**, *21*, No. 084204.

(30) Taylor, C. D.; Wasileski, S. A.; Filhol, J.-S.; Neurock, M. First Principles Reaction Modeling of the Electrochemical Interface: Consideration and Calculation of a Tunable Surface Potential from Atomic and Electronic Structure. *Phys. Rev. B: Condens. Matter Mater. Phys.* **2006**, *73*, 165402.

(31) Filhol, J.-S.; Neurock, M. Elucidation of the Electrochemical Activation of Water over Pd by First Principles. *Angew. Chem., Int. Ed.* **2006**, *45*, 402−406.

(32) Mathew, K.; Sundararaman, R.; Letchworth-Weaver, K.; Arias, T. A.; Hennig, R. G. Implicit Solvation Model for Density-Functional Study of Nanocrystal Surfaces and Reaction Pathways. *J. Chem. Phys.* **2014**, *140*, No. 084106.

(33) Fishman, M.; Zhuang, H. L.; Mathew, K.; Dirschka, W.; Hennig, R. G. Accuracy of Exchange-Correlation Functionals and Effect of Solvation on the Surface Energy of Copper. *Phys. Rev. B: Condens. Matter Mater. Phys.* **2013**, *87*, 245402.

(34) Nørskov, J. K.; Rossmeisl, J.; Logadottir, A.; Lindqvist, L.; Kitchin, J. R.; Bligaard, T.; Jónsson, H. Origin of the Overpotential for Oxygen Reduction at a Fuel-Cell Cathode. *J. Phys. Chem. B* **2004**, *108*, 17886−17892.

(35) Hansen, H. A.; Rossmeisl, J.; Nørskov, J. K. Surface Pourbaix Diagrams and Oxygen Reduction Activity of Pt, Ag and Ni(111) Surfaces Studied by DFT. *Phys. Chem. Chem. Phys.* **2008**, *10*, 3722.

(36) He, Z.-D.; Hanselman, S.; Chen, Y.-X.; Koper, M. T. M.; Calle-Vallejo, F. Importance of Solvation for the Accurate Prediction of Oxygen Reduction Activities of Pt-Based Electrocatalysts. *J. Phys. Chem. Lett.* **2017**, *8*, 2243−2246.

(37) Kerr, J. A. Bond Dissociation Energies by Kinetic Methods. *Chem. Rev.* **1966**, *66*, 465−500.

(38) Liu, H.; Liu, Y.; Zhu, D. Chemical doping of graphene. *J. Mater. Chem.* **2011**, *21*, 3335−3345.

(39) Xue, L.; Li, Y.; Liu, X.; Liu, Q.; Shang, J.; Duan, H.; Dai, L.; Shui, J. Zigzag carbon as efficient and stable oxygen reduction electrocatalyst for proton exchange membrane fuel cells. *Nat. Commun.* **2018**, *9*, 3819.

(40) Wu, J.; Ma, L.; Yadav, R. M.; Yang, Y.; Zhang, X.; Vajtai, R.; Lou, J.; Ajayan, P. M. Nitrogen-Doped Graphene with Pyridinic Dominance as a Highly Active and Stable Electrocatalyst for Oxygen Reduction. *ACS Appl. Mater. Interfaces* **2015**, *7*, 14763−14769.

(41) Ning, X.; Li, Y.; Ming, J.; Wang, Q.; Wang, H.; Cao, Y.; Peng, F.; Yang, Y.; Yu, H. Electronic synergism of pyridinic- and graphitic-nitrogen on N-doped carbons for the oxygen reduction reaction. *Chem. Sci.* **2019**, *10*, 1589−1596.